

Heat-Resistant Molybdenum Borosilicate Alloys Hardened with Titanium Carbides: Mo–Si–B–TiC (Survey)

I. L. Svetlov^{a,*}, O. G. Ospennikova^a, M. I. Karpov^b, and Yu. V. Artemenko^a

^a All-Russian Scientific Research Institute of Aviation Materials, Moscow, 105005 Russia

^b Institute of Solid State Physics, Russian Academy of Sciences, Chernogolovka, 142432 Russia

*e-mail: i.svetlov2010@yandex.ru

Received March 10, 2020; revised April 22, 2020; accepted May 19, 2020

Abstract—The review article is devoted to high-temperature borosilicate molybdenum alloys reinforced with titanium carbides MoSiBTiC. The article discusses phase diagrams, microstructure, production methods, mechanical properties, resistance to oxidation of these alloys, and protective coatings. It is shown that the long-term strength of MoSiBTiC alloys is superior at high temperatures to nickel heat-resistant alloys (NHRA) of the latest generations. Borosilicate molybdenum alloys MoSiBTiC can replace nickel heat-resistant alloys in many engineering fields, including in the production of cast parts for the hot section of aircraft gas turbine engines.

Keywords: borosilicate molybdenum alloys, production, structure, mechanical properties, heat resistance, protective coatings

DOI: 10.1134/S2075113321040432

INTRODUCTION

Presently, it is becoming more and more obvious that cast nickel heat-resistant alloys (NHRA) with heat-shielding coatings have exhausted their potential possibilities in relation to increasing the operating temperature of single-crystal blades made of these alloys. This circumstance served as the motivation for writing a review article on new high-melting materials for structural purposes based on the Mo–Si–B system.

When assessing the ability of heat-resistant metal materials to withstand certain mechanical loads at high temperatures, the concept of homologous temperature $\theta = T_c/T_m$ is used, which characterizes the property of the material. In this expression, T_m is melting point of the material and T_c is the temperature at which the material retains its working capacity and withstands long-term loads.

In modern gas turbine engines, homologous temperatures of rotor blades of the first stage of a high-pressure turbine reach $\theta = T_c/T_m \approx 0.85$, i.e., 85% of the melting point of the alloy T_m , which corresponds to the limiting temperature $T_c \geq 1175^\circ\text{C}$. There are two possibilities of lowering θ : either by more efficient cooling of working blades [1] and thereby reducing T_c or by manufacturing blades from new heat-resistant high-melting materials with melting point $T_m \geq 2000^\circ\text{C}$ [2–4]. At the same time, such materials should have low rates of high-temperature creep, high heat resistance, reliable protective coatings, and low density. The charac-

teristics of multicycle fatigue and crack resistance are of great importance, as well as the development of a cost-effective technology for production of parts from new high-melting materials.

Since 2013, every three years, international conferences are held on the search for and development of high-temperature heat-resistant alloys that can replace cast nickel alloys in the production of parts for the hot-path GTE (Beyond Nickel-Based Superalloys) [5–7]. The third such conference was held in June 2019 in Japan. There were reports on the following topics:

1. Molybdenum Mo–Si and niobium Nb–Si alloys.
2. Cobalt alloys.
3. Eutectic composites (Cr–V–Si, MoSi₂/Mo₃Si₃, V–Si–B, NiAl–(CrMo)).
4. High-entropy alloys.
5. Alternative alloys.

If we analyze the topics of reports at all conferences, we can note that the largest number of reports are devoted to the development of alloys based on high-melting metals, in particular, molybdenum alloys of the Mo–Si–B system, and to a lesser extent niobium alloys of the Nb–Si system.

Currently, development and research of new molybdenum alloys is not carried out in Russia and therefore it is advisable to review the methods of obtaining high-heat-resistant borosilicate molybdenum alloys MoSiBTiC for structural purposes, their

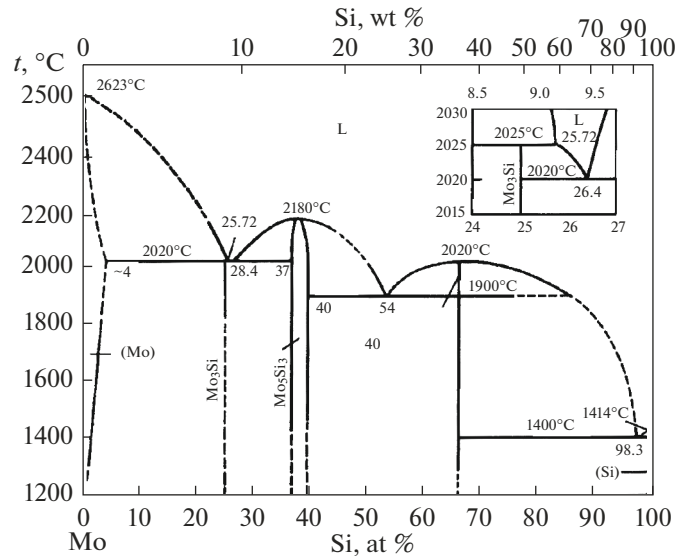


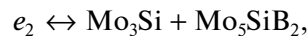
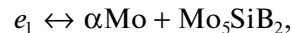
Fig. 1. Binary diagram of Mo–Si.

microstructure, phase composition, mechanical properties up to temperatures of 1400°C, heat resistance, and most importantly resistance to high-temperature oxidation and protective coatings. These issues are considered to a greater or lesser extent in this article. Similar review articles devoted to high-temperature composites based on the Nb–Si system were published in the journals *Materials Science* [8] and *Metal Science and Heat Treatment* [9]. Review articles have also appeared in foreign periodicals, in particular, “Mo–Si–B Alloys for Ultra-High Temperature Structural Application” by the authors Lemberg and Ritchie [10] and “Research Trends of the Mo–Si–B Alloys as Next Generation Ultra-High Temperature Alloys” by a team of Korean authors [11]. The work was carried out within the framework of the implementation of the complex scientific direction 9.4.2. “Composites Based on High-Melting Metals, Reinforced with Intermetallic Compounds” (“Strategic Directions for the Development of Materials and Technologies for Their Processing for the Period up to 2030”) [12].

PHASE DIAGRAMS OF Mo–Si, Mo–Si–B, AND Mo–Si–B–TiC

At first, it is advisable to consider the structure of the phase diagrams, on the basis of which the compositions of molybdenum alloys in the Mo–Si–B system are selected and the phase stability of the microstructure of such alloys at high temperatures is estimated. Figure 1 shows the well-known binary Mo–Si diagram, and Fig. 2 shows the isothermal section in the molybdenum corner of the Mo–Si–B ternary diagram at a temperature of 1600°C constructed for the first time by Novotny [13]. For a better understanding of

the formation of the microstructure during crystallization of alloys, the projections of liquidus surfaces are superimposed on the isothermal section [14]. Further, we will be mainly interested in the α Mo–Mo₃Si–Mo₅SiB₂ phase triangle (the Mo₅SiB₂ phase is often denoted as T₂), sometimes called the Berczik triangle [15, 16]. The chemical compositions of most of the developed borosilicate molybdenum alloys for structural purposes lie within this triangle or near its boundaries. Experimental results and thermodynamic calculations [17] of the structure of Berczik triangle indicate the presence in it of two double and one triple phase region formed by eutectic reactions:



Thus, most molybdenum alloys in the Mo–Si–B system contain the three indicated phases—a solid solution of molybdenum α Mo and silicides Mo₃Si and T₂, in which various alloying elements dissolve to one degree or another to give alloys certain properties. The chemical composition of the ternary eutectic *E* is approximately equal to Mo–(16–18) Si–(7–8) B (at %), its phase composition consists of 50% α Mo, 30% Mo₃Si, and 20% T₂, and the temperature of the ternary eutectic is \approx 1900–2000°C [18, 19]. The chemical compositions of binary eutectics *e*₁ and *e*₂ are approximately equal to Mo–8Si–14B (at %) and Mo–20Si–7B (at %), respectively [20].

The evolution of the microstructure and reaction during crystallization of alloys in the molybdenum corner of the Mo–Si–B diagram was studied in detail [21]. Fifty-nine alloys were analyzed in the vicinity of

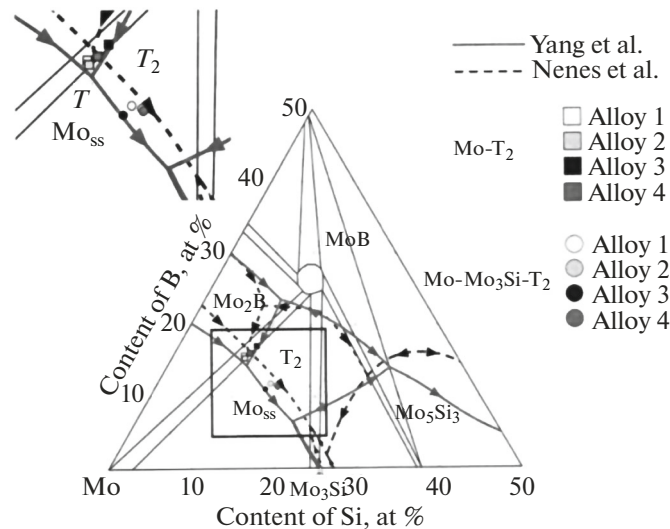


Fig. 2. Isothermal cross section of ternary diagram of Mo–Si–B at 1600°C (dashed lines with arrows are projections of liquidus lines).

the triple eutectic point $\alpha\text{Mo}-\text{Mo}_3\text{Si}-\text{T}_2$. Experimental results confirmed thermodynamically calculated positions of the liquidus projection. Particular attention was paid to the primary crystallization of the Mo_3Si phase and the $\alpha\text{Mo}-\text{Mo}_3\text{Si}-\text{T}_2$ ternary eutectic, the refined composition of which was determined as 17 at % Si and 7.5 at % B.

Let us consider phase equilibria in alloys of the Mo–Si–B system doped with titanium carbide TiC and denoted in the literature as MoSiBTiC [22]. To construct diagrams of the state of such high-temperature materials, a method of thermal analysis using electromagnetic levitation was specially developed, which excludes high-temperature chemical interaction of the investigated melts with the crucible material. In addition, the method made it possible to optically observe in situ the evolution of the microstructure during crystallization of the alloy [23].

Figure 3 shows the cooling curve of an alloy with the composition 67.5Mo–5Si–10B–8.75Ti–8.75C (at %). It has 5 inflection points *a–e*. Using thermal analysis data and the results of in situ microstructural studies, it was possible to construct a crystallization path for this alloy. Table 1 implies that the formed structure contains three phases— $\alpha\text{Mo}_{\text{ss}}$, Mo_2B , and T_2 , one binary eutectic $\text{Mo}_{\text{ss}} + \text{TiC}$, and two ternary eutectics $\text{Mo}_{\text{ss}} + \text{T}_2 + \text{TiC}$ and $\text{Mo}_{\text{ss}} + \text{T}_2 + \text{Mo}_2\text{C}$.

The obtained data were used to construct a quadruple phase diagram of the Mo–Si–B–TiC alloy (Fig. 4). The chemical composition of the alloy is indicated by a dot * on the diagrams in Figs. 4a–4c. The investigated alloy in the ternary diagram Mo– T_2 –TiC has the composition 75.6Mo–8.9B (T_2)–15.6TiC (at %) and its position is also indicated in Fig. 4b.

In the ternary diagram, the composition of the alloy under study is in the region where Mo is the first

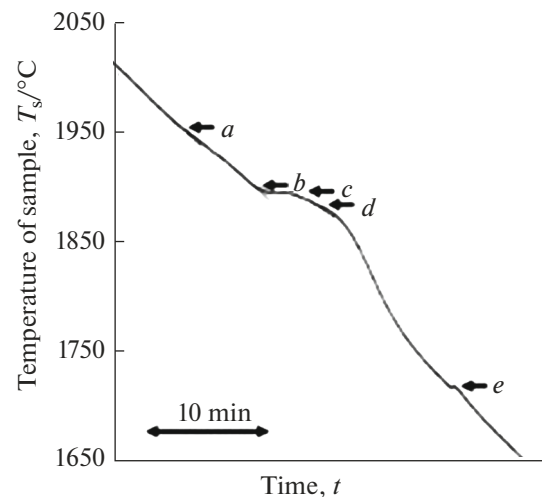


Fig. 3. Curve of cooling of alloy 67.5Mo–5Si–10B–8.75Ti–8.75C (at %).

Table 1. Crystallization path of alloy 67.5Mo–5Si–10B–8.75Ti, 8.75C (at %)

Inflection points	Temperature, °C	Reactions
<i>a</i>	1995	$\text{Liq} \rightarrow \text{Mo}_{\text{ss}}$
<i>b</i>	1900	$\text{Liq} \rightarrow \text{Mo}_{\text{ss}} + \text{TiC}$ eutectic
<i>c</i>	1894	$\text{Liq} \rightarrow \text{Mo}_2\text{B}$
		$\text{Liq} + \text{Mo}_2\text{B} \rightarrow \text{Mo}_{\text{ss}} + \text{T}_2$
<i>d</i>	1880	$\text{Liq} \rightarrow \text{T}_2$
		$\text{Liq} \rightarrow \text{Mo}_{\text{ss}} + \text{T}_2 + \text{TiC}$ eutectic
<i>e</i>	1720	$\text{Liq} \rightarrow \text{Mo}_{\text{ss}} + \text{T}_2 + \text{Mo}_2\text{C}$ eutectic

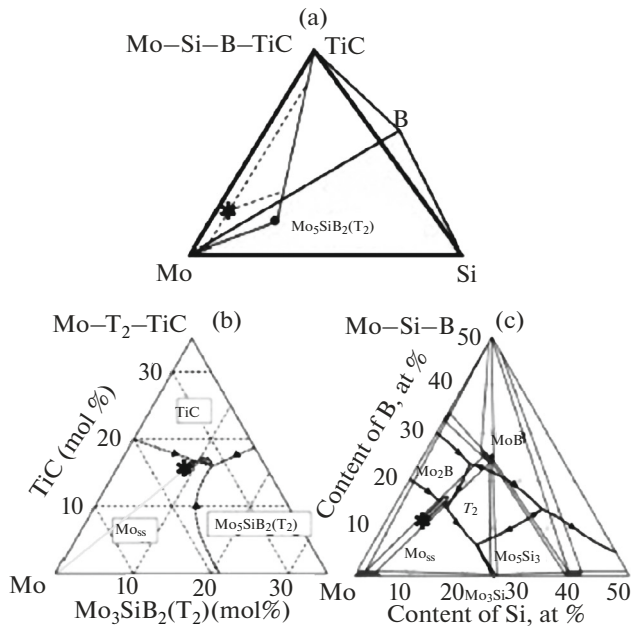


Fig. 4. Quaternary phase diagram of Mo–Si–B–TiC (a); ternary phase diagram of Mo–T₂–TiC (b), ternary phase diagram of Mo–Si–B (c).

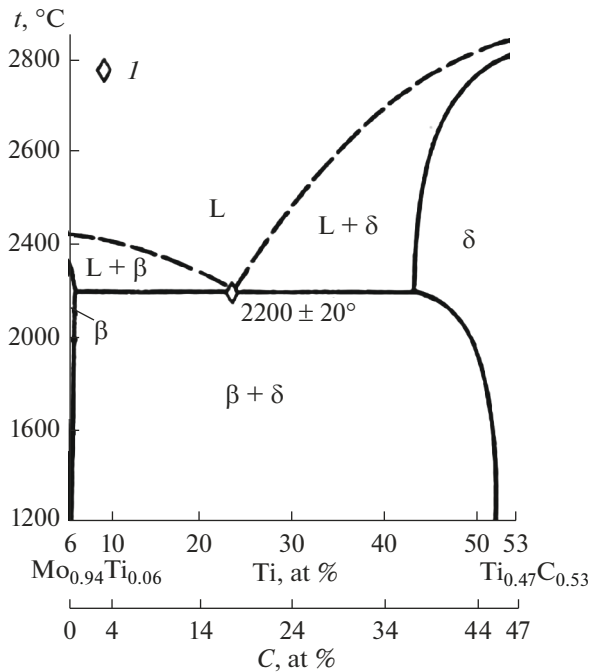


Fig. 5. Quasi-binary section of Mo_{0.94}Ti_{0.06}–Ti_{0.53}C_{0.47} in diagram of Mo–Ti–C.

to be released. Thus, after separation of primary Mo at the temperature of 1955°C (point *a* in Table 1), the composition of the melt changes in the direction toward the Mo/TiC interface and then to the point of the binary eutectic at 1900°C $\text{Liq} \rightarrow \text{Mo}_{\text{ss}} + \text{TiC}$ (point *b*). It is necessary to note that, when developing

this alloy, the authors used a partially quasi-binary section Mo–TiC in the ternary diagram Mo–Ti–C constructed by V.N. Eremenko and T.Ya. Velikanova in 1985 [24]. It can be seen in Fig. 5 that the diagram in this section has a eutectic form at the temperature of 2175°C and composition of 23TiC (at %), while the authors of [12] determined the eutectic temperature as 1900°C in the quaternary diagram of Mo–Si–B–Ti–C.

In Fig. 4c, the initial composition of the alloy is projected onto the basal plane of the Mo–Si–B diagram and is located in the two-phase region of Mo–T₂.

As crystallization proceeds, the content of Mo in the melt decreases owing to the eutectic reaction and the composition of the melt shifts to the region of primary separation of the Mo₂B phase, which reacts with the melt to form two phases Mo and T₂:

$\text{Liq} + \text{Mo}_2\text{B} \rightarrow \text{Mo} + \text{T}_2$ at the temperature of 1984°C (point *c*).

The T₂ phase can also be independently separated from the melt. At the final stage, the remaining melt crystallizes with formation of ternary eutectic structures:

$\text{Liq} \rightarrow \text{Mo} + \text{T}_2 + \text{TiC}$ at 1880°C (point *d*),

$\text{Liq} \rightarrow \text{Mo} + \text{T}_2 + \text{Mo}_2\text{C}$ at 1720°C (point *e*).

In this way, MoSiBTiC alloys have a more complex phase composition than three-component MoSiB alloy and after casting contain the following phases: $\alpha\text{Mo} + \text{Mo}_5\text{SiB}_2 + \text{TiC} + \text{Mo}_2\text{C}$.

Before analyzing the specific properties of MoSiBTiC alloys, it is advisable to characterize the main properties of individual phases αMo , Mo₃Si, Mo₅SiB₂ (T₂), and Mo₅Si₃ (T₁).

Molybdenum is intensely oxidized above a temperature of 500°C and MoO₃ oxide film easily volatilizes. The strength and ductility of BCC solid solution αMo depends on impurities and alloying elements. It is well known that the main solid-solution strengthening element of αMo is silicon, which segregates at dislocation cores and grain boundaries and thus embrittles molybdenum alloys. On the contrary, zirconium and spinel MgAl₂O₄ increase the plasticity of Mo.

Intermetallic Mo₃Si has lower heat resistance than molybdenum disilicide MoSi₂, has A15 cubic structure, is rather brittle, and has a large anisotropy of elastic constants. It is susceptible to corrosion at medium temperatures. When doped with aluminum, the oxidation resistance increases.

Intermetallic Mo₅Si₃ (T₁) has high anisotropy of the coefficient of linear thermal expansion (CLTE) and therefore cracks upon cooling, has a tetragonal lattice, and has low heat resistance. Boron increases oxidation resistance. Above 1300°C, single crystals of silicide Mo₅Si₃ (T₁) acquire plasticity upon compression.

Table 2. Some properties of molybdenum silicides

Property	Mo ₃ Si	Mo ₅ Si ₃	MoSi ₂
Content of Si, wt %	9.18	14.94	36.88
Melting point (T_{melt}), °C	2025	2180	2020
Heat of formation (H_{298}°), kJ/mol	102.6	94.6	54.4
CLTE (α) 10^{-6} , K ⁻¹ (20–1070°C)	3.4–6.5	4.3–6.7	8.25–9.2
Resistance (ρ), $10^8 \Omega \text{ m}$	21.6	46.7	21.6
Thermo EMF (S), 10^6 V/K	–1.0	2.0	–3.0
Young's modulus (E), 10^{12} Pa	30.90 ± 0.98	–	44.14 ± 0.49
Shear modulus (G), 10^4 Pa	96138	1029890	137293

Intermetallic Mo₅SiB₂ (T₂) has a body-centered tetragonal lattice and possesses high heat resistance, and there are limited data on mechanical properties, in particular, high-temperature creep at 1300°C.

Some properties of molybdenum silicides are given in Table 2 [25]. A more detailed description of the properties of individual phases is given in the review article by Lemberg and Ritchie [10].

METHODS TO OBTAIN MoSiBTiC ALLOYS

To obtain molybdenum alloys MoSiBTiC in laboratory conditions, various methods are used, namely, metallurgy of slits, directional crystallization, mechanical alloying, powder metallurgy, and additive technologies. However, a cost-effective industrial technology for smelting and manufacturing of complex parts from them has not yet been developed. The most common are the simple metallurgical method of smelting ingots by vacuum arc melting (VAM) with a nonconsumable electrode and inclined casting [26]. For smelting, powders of molybdenum, silicon, and boron are used, as well as alloying elements of high purity and compressed powder of titanium carbide TiC. Owing to the high melting temperature of the alloys $\approx 2000^\circ\text{C}$ and the tendency of boron to form segregations during crystallization, unwanted borides MoB and Mo₂B can be released. Stirring of the melt in the VAR method is absent and, as a result, there is a significant chemical heterogeneity throughout the thickness of the plate. Therefore, it is necessary to turn the plate over several times and carry out repeated recrystallization for a more uniform distribution of alloying elements. Another disadvantage of the VAR method is small weight of the ingots $\approx 100\text{--}200 \text{ g}$. However, by simultaneously alloying several small ingots by the induction method in an oxide crucible, one can obtain an ingot weighing up to 3.5 kg with polycrystalline structure [27].

Directional crystallization is used to obtain an oriented compositional structure of molybdenum alloys. The patent [28] describes the design of an installation

for directional crystallization of high-melting Mo and Nb alloys by the Bridgman–Stockbarger method in “cold” crucibles. Directional crystallization is carried out by pulling out a segmented water-cooled copper crucible with melt from a high-frequency inductor. Owing to electromagnetic levitation, the melt is in a suspended state and slightly contacts the walls of the crucible. For research purposes, small samples with directed structure are obtained in laboratory facilities by the floating zone method [29].

Directional crystallization of Mo–17.5Si–(8–10)B molybdenum alloys, close in composition to the ternary eutectic, was carried out by the floating zone method with a growth rate of 60 mm/h [30]. At such high crystallization rates, the criterion of a flat growth front is violated and, therefore, there is no directional orientation of the structure and, consequently, no effect of compositional hardening.

At Plansee AG, industrial powder technology was used to produce a molybdenum alloy of chemical composition Mo–8.9Si–7.7B [31]. The alloy contained three phases, Mo–T₂ – Mo₃Si, and had good chemical homogeneity and the same level of impurities as conventional industrial molybdenum alloys.

As one of the options for powder metallurgy, mechanical alloying in attritors is often used to prepare samples of the Mo–Si–B molybdenum alloy additionally alloyed with Zr, La₂O₃, SiC, and ZrC. In [32–34], the effect of zirconium on the microstructure, strength, and fracture resistance of samples obtained by mechanical alloying followed by hot pressing was studied. It is shown that alloying with zirconium increases the hardness, compressive strength, and especially fracture resistance. Zirconium has a refining effect and forms fine particles of ZrO₂ in the bulk and along the boundaries of molybdenum grains. During destruction, microcracks propagate along the interfaces between oxide particles and molybdenum—ZrO₂/Mo. In addition, mechanical alloying lowers by 150°C the transition temperature from brittle to ductile fracture and at the same time slightly increases the ductility at 954°C.

The authors of [35, 36] investigated the heat resistance of alloys of the Mo–Si–B system obtained by mechanical alloying from powders followed by consolidation by hot pressing at temperatures of 800 and 1000°C. It is shown that, after hot pressing, the material consists of three phases: solid solution αMo , molybdenum silicide Mo_3Si (A15), and molybdenum borosilicide Mo_5SiB_2 (T_2). It was also established that annealing at temperature of 800 and 1000°C for 2 h leads to a decrease in the mass of the material due to evaporation of the surface layer of the material of molybdenum trioxide MoO_3 , and no mass change after holding for more than 2 h is explained by the formation of a protective film based on borosilicate glass.

The influence of rare earth elements, in particular, lanthanum oxide La_2O_3 , on the microstructure and mechanical properties of Mo–12Si–8.5B alloys prepared by mechanical alloying followed by hot pressing was studied in detail in [37, 38]. These articles confirmed the previously obtained results on the effect of nanosized La_2O_3 particles on compressive strength and fracture resistance.

The authors of [39] made an attempt by the method of mechanical alloying to carry out additional hardening of a multiphase alloy of composition Mo–12Si–8.5B with whiskers of silicon carbide SiC. However, the expected increase in strength due to the contribution of whiskers was not obtained because of arbitrary orientation of the whiskers.

Multistage powder technologies are not profitable for mass production of complex parts such as GTE blades. Therefore, great hopes are pinned on single-stage technologies for manufacturing complex parts from such alloys, for example, additive technologies. Over the past two years, several articles have appeared which describe the process of making powders of the Mo–Si–B–TiC alloy followed by laser synthesis of the resulting powders.

In [40], a method for producing powders in two stages is described. At first, the alloy ingot is melted by the VAM method and then controlled crushing is carried out in high-energy planetary mills. The shape change of the powder particles, their phase composition, and the size distribution of the powder particles in the process of crushing were investigated. In addition, the influence of the crushing parameters on compaction, microstructure, and mechanical properties of the alloy was studied. The phase composition of the alloy was determined, which consisted of Mo solid solution, Mo_5SiB_2 silicide, and Mo_2C and TiC carbides. Compared to cast alloy, the synthesized alloy had a more uniform fine-grained structure, but a lower Vickers hardness.

For the first time, for laser deposition, the suitability of a powder close in composition to the ternary eutectic Mo–13.5Si–7.5B and obtained by gas spraying was determined [41, 42]. The composition of particles, size distribution, their sphericity, state of the

surface, and impurities were studied. The microstructure of the sample and its phase composition were investigated: primary precipitates αMo , binary eutectic $\text{Mo}_3\text{Si} + \text{Mo}_5\text{SiB}_2$, and ternary eutectic $\alpha\text{Mo} + \text{Mo}_3\text{Si} + \text{Mo}_5\text{SiB}_2$. High porosity was observed.

An original method of using carbon nanotubes for the in situ synthesis of TiC–Mo composite by laser powder deposition is described in [43]. Carbon nanotubes treated in nitric acid were dispersed together with MoTiAl powder with formation of heteroagglomeration under the impact of electrostatic attraction. During laser spraying, carbon nanotubes react with titanium atoms and are completely converted into TiC carbide. Titanium carbide had two morphologies, small-spherical and dendritic, and formed a tight contact with the matrix. Composites obtained by this method possessed increased hardness.

Molybdenum alloy of composition Mo–8.5Si–5.6B (at %), which had dendritic structure αMo , was obtained by the laser method and two-phase mixture Mo_5Si_3 (T_1) + Mo_5SiB_2 (T_2) was found in interdendrite space instead of the expected two-phase mixture $\text{Mo}_3\text{Si} + \text{Mo}_5\text{SiB}_2$ [44]. Such a nonequilibrium structure was retained after annealing at 1200°C for 200 h. The authors explain formation of a nonequilibrium structure by strong supercooling of the melt during laser sintering. Introduction of dispersed La_2O_3 particles increased fracture resistance of the alloy to $18 \text{ MPa m}^{1/2}$.

CHEMICAL AND PHASE COMPOSITIONS OF ALLOYS. MICROSTRUCTURE

Compared to nickel heat-resistant alloys, the alloying complex of molybdenum alloys MoSiBTiC is much simpler and does not contain scarce and expensive elements such as rhenium and ruthenium. The chemical composition of MoSiBTiC alloys is presented in Table 3.

The following phases were found in the cast structure of the molybdenum alloy of generation I: solid solution αMo , silicide Mo_5SiB_2 (T_2), and carbides $(\text{Mo}, \text{Ti})_2\text{C}$ and $(\text{Ti}, \text{Mo})\text{C}$, as well as two-component and three-phase eutectic components $\text{Mo} + (\text{Ti}, \text{Mo})\text{C}$, $\text{Mo} + (\text{Ti}, \text{Mo})\text{C} + T_2$, $\text{Mo} + (\text{Mo}, \text{Ti})_2\text{C} + T_2$. During high-temperature annealing at 1800°C for 24 h, metastable carbide $(\text{Mo}, \text{Ti})_2\text{C}$ is decomposed into αMo and $(\text{Ti}, \text{Mo})\text{C}$, and after homogenization, the number of phases is reduced to three at the following ratio: $\alpha\text{Mo} \approx 46\%$, $T_2 \approx 36\%$, and $(\text{Ti}, \text{Mo})\text{C} \approx 18\%$ [45]. In the same article, the orientation relation between molybdenum and silicides T_2 as well as between molybdenum and carbides $(\text{Ti}, \text{Mo})\text{C}$ is determined:

$$\{1\bar{1}0\}_{\text{Mo}} // (001)_{T_2}, \langle 111 \rangle_{\text{Mo}} // \langle 111 \rangle_{T_2}, \\ \{1\bar{1}0\}_{\text{Mo}} // \{111\}_{(\text{Ti}, \text{Mo})\text{C}}, \langle 111 \rangle_{\text{Mo}} // \langle 110 \rangle_{(\text{Ti}, \text{Mo})\text{C}}.$$

Figure 6 shows the 3D SEM microstructure of the first generation of MoSiBTiC molybdenum alloy,

which illustrates the morphology and approximate volume ratio of alloy phase components— α Mo solid solution, TiC carbides, and Mo_5SiB_2 (T_2) silicides.

The chemical and phase composition of the second generation of MoSiBTiC alloys differs from the first generation in the presence of chromium, a higher content of titanium and silicon, and the appearance of a new silicide phase Ti_5Si_3 . As a result of the optimization of the composition of the second generation alloys, they possess lower density and accordingly higher specific strength. The second generation alloys contain 4 phases— α Mo, silicides Mo_5SiB_2 (T_2), a new phase Ti_5Si_3 , and TiC carbides. Formation of titanium silicide Ti_5Si_3 increased the resources of silicon in the microstructure and as a consequence high-temperature heat resistance, and doping with chromium increased the resistance to oxidation at temperature of 800°C owing to formation of a protective layer of chromium oxide [46].

In alloyed systems Mo–Si–B–X, where X is TiC, SiC, La_2O_3 , Zr, combined hardening is realized: solid phase hardening of α Mo, intermetallic silicide Mo_5SiB_2 (T_2), and rare earth metals dispersed with carbides or rare oxides. Alloyed multiphase MoSiBTiC alloys are characterized by a varied structure of interfaces between different phases. Therefore, when analyzing the mechanical properties and studying the mechanisms of destruction of alloys, it is important to know the structure of the interfaces between the solid solution of molybdenum, silicides, and various carbide phases. In [47], the atomic structure of stepwise interface $\alpha\text{Mo}-(\text{Ti}, \text{Mo})\text{C}-(\text{Mo}, \text{Ti})_2\text{C}$ was investigated by direct resolution TEM and it was shown that the interphase boundaries are consistent.

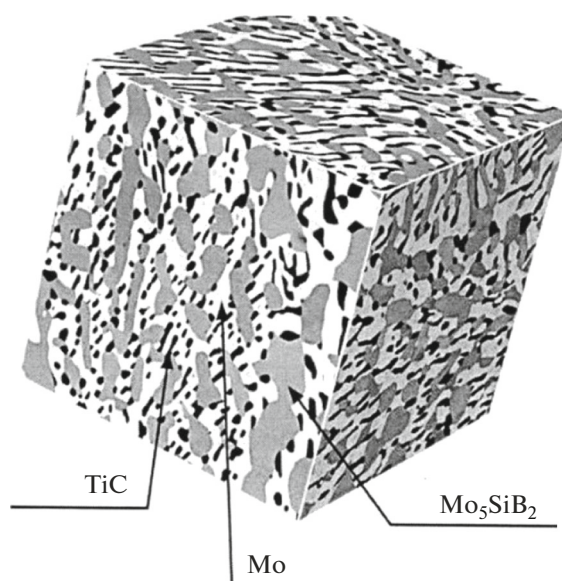


Fig. 6. 3D SEM microstructure of alloy MoSiBTiC of I generation.

MECHANICAL PROPERTIES OF MoSiBTiC ALLOYS

Elastic Moduli and Short-Term Mechanical Properties

Borosilicate alloys of molybdenum hardened with titanium carbides were developed as structural materials with consistently high mechanical properties in a wide temperature range. Presently, it has been reliably established that the strength of alloys significantly depends on the values of the elastic moduli, which are used in computing the structural strength of various parts. The elastic moduli of the Mo–8.9Si–7.7B alloy

Table 3. Systems of alloying of molybdenum alloys Mo–Si–B–TiC and NHRA

No.	Alloy	Alloying system	Chemical composition, at %						Phase composition	T_{melt} , $^\circ\text{C}$	d , g/cm^3
			Mo	Si	B	Ti	C	Cr			
1	Mo I generation	Mo–Si–B–TiC	65	5	10	10	10	–	$\alpha\text{Mo} + T_2 + (\text{Ti}, \text{Mo})\text{C}$	1920	8.8
2	Mo II generation	Mo–Si–B–TiC–Cr	36	14	6	28	6	10	$\alpha\text{Mo} + T_2 + \text{Ti}_5\text{Si}_3 + (\text{Ti}, \text{Mo})\text{C}$	1920	7.1
3	Mono NHRA of generation V	Ni–Al–Cr–Mo–W–Ta–Co–Re–Ru	–	–	–	–	–	–	γ/γ'	1370	≥ 9

Table 4. Elastic moduli of alloy Mo–12Si–8.5B in the range of $24-1200^\circ$

Temperature, T , $^\circ\text{C}$	Young's modulus E , GPa	Shear modulus G , GPa	Volume modulus B , GPa	Poisson coefficient, ν
24	325	125	252	0.285
300	313	121	248	0.289
600	298	115	241	0.294
900	284	109	241	0.304
1200	269	102	239	0.312

Table 5. Temperature dependence of alloy Mo–8.9Si–7.7B

State	Temperature, T , °C	Creep limit, $\sigma_{0.2}$, MPa	Tensile strength, σ_b , MPa	Elongation ϵ , %
HIP	538	—	412	0
	816	—	423	0
	1093	—	424	0
	1200	335	450	7.3
Extrusion	538	—	639	0
	816	—	677	0
	1093	666	722	21.5

were computed by the finite element method and experimentally determined by the resonance method [48]. The numerical values of these modules at different temperatures are presented in Table 4.

The tensile strength properties of the Mo–8.9Si–7.7B alloy in the temperature range of 538–1200°C in vacuum are presented in Table 5 [49].

The graph (Fig. 7) shows the average values of the ultimate strength σ_b , yield $\sigma_{0.2}$, and elongation ϵ of samples of the same alloy at various temperatures up to 1600°C. Samples 15 and 3 mm in diameter fractured in a brittle manner below 1100°C, and at 1200°C, elongation at fracture was 5%. Consequently, the brit-

tle–ductile fracture transition temperature is in the range of 1150–1200°C. Increase in temperature beyond the upper limit causes significant elongation with simultaneous decrease in the ultimate strength and yield strength [50].

For comparison, Fig. 7b shows the graphs of temperature dependence of strength and plasticity of NHRA single crystals in [001] orientation and Mo–8.9Si–7.7V molybdenum alloy. It can be seen that above 1150°C, the molybdenum alloy is stronger than NHRA single crystals.

Long-Term Strength and Creep

The long-term strength of MoSiBTiC alloys at high temperatures, in particular, high-temperature creep under tension, was investigated in more detail [51–54]. Figure 8 presents the creep curves of 65Mo–5Si–10V–10TiC molybdenum alloy of the first generation in coordinates of creep strain–time $\epsilon = f(\tau)$ at temperatures of 1400, 1500, and 1600°C in vacuum [51].

Table 6 shows numerical values of the long-term strength of some cast heat-resistant alloys based on nickel, niobium, and molybdenum. Analysis of the data in the table allows making the following conclusions:

(1) Molybdenum alloys have a simple alloying system and do not contain heavy and expensive alloying elements such as rhenium and ruthenium.

(2) The density of molybdenum alloys is equal to that of NHRA of the last generation, but higher than the density of VKNA and alloys of Nb–Si system.

(3) At high temperatures, the heat resistance of molybdenum alloys significantly surpasses the known NHRA with satisfactory long-term ductility. A clear advantage of molybdenum alloys in comparison with single crystals of NHRA of the last generation follows from consideration of the Larsen–Miller parametric dependence (Fig. 9). At large values of the Larsen–Miller parameters LMP (high temperatures and long service lives), the heat resistance of polycrystalline molybdenum alloys significantly exceeds that of single-crystal NHRA VZhM-4. Unfortunately, in the region of low LMP values, i.e., at medium temperatures, there are no experimental data for molybdenum

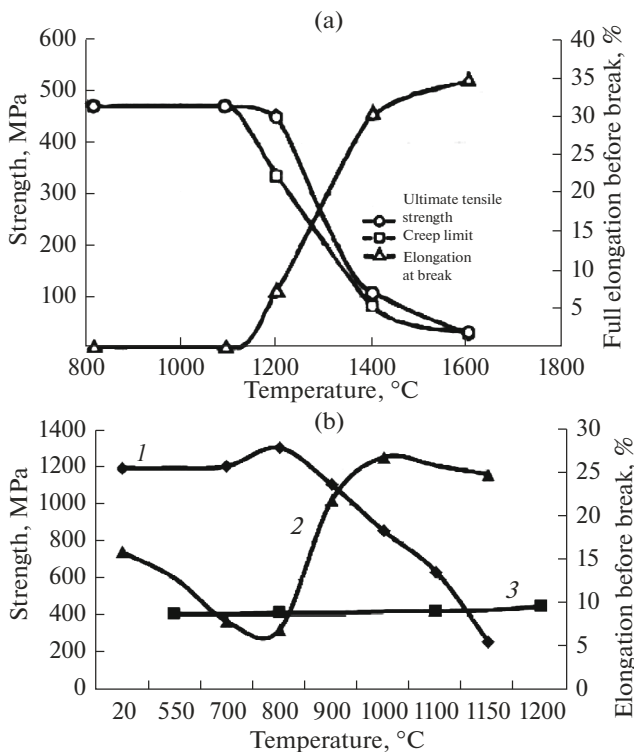


Fig. 7. Temperature dependence of strength of molybdenum alloy and NHRA: (a) molybdenum alloy Mo–8.9Si–7.7B; (b) NHRA; (1) tensile strength; (2) elongation; (3) tensile strength of Mo–8.9Si–7.7B.

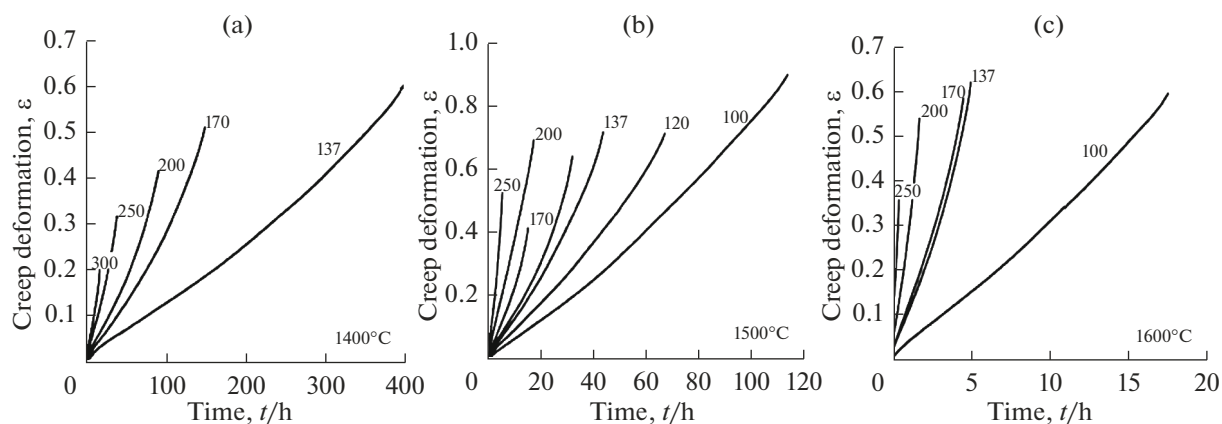


Fig. 8. Creep curves of alloy 65Mo–5Si–10B–10TiC at temperatures of 1400 (a), 1500 (b), and 1600°C (c) and stresses in the range of 100–300 MPa.

alloys. Therefore, we will use the conditional assumption that, in the range of temperatures of 538–1200°C and the ultimate strength of alloy of ≈ 412 –450 MPa (see Table 5), the fatigue life of the alloy is 0.1 h [55]. Then Larsen–Miller curve for the molybdenum alloy can be extrapolated to small values of the parameters LMP (see the last four points on the graph in Fig. 9). It can be seen that the curves intersect: to the right of the intersection point, the heat resistance of MoSiBTiC molybdenum alloy exceeds that for single crystals of NHRA VZhM-4 and to the left of the intersection point, on the contrary, NHRA single crystals have a higher heat resistance.

For a phenomenological description of the process of high-temperature creep of the alloy, we used the known dependence of the minimum creep rate $\dot{\epsilon}$ on stresses σ and temperature T :

$$\dot{\epsilon} = A\sigma^n \exp\left(-\frac{Q}{RT}\right),$$

where the power exponent $n = 3$ and activation energy at the minimum creep rate is $Q = 550$ kJ/mol. In Table 7, these values are compared with the published data for pure Mo and molybdenum alloys after tests for creep

under tension and compression and with a constant strain rate, as well as data on self-diffusion of molybdenum. It can be seen that there is a very large scatter in the creep activation energy of 318–740 kJ/mol depending on the composition of alloys, type of testing, and the temperature range. The value of the activation energy of 550 kJ/mol determined in this article coincides with the data for tension and compression of 560 kJ/mol (see rows 6 and 7 in Table 7) and exceeds the activation energy of self-diffusion of molybdenum, which is equal to 460 kJ/mol.

As for the constant n , the table values change in a smaller range of 2–5.5 and the article gives the value $n = 3$. Presently, it is believed that n has no definite physical meaning, although it was previously associated with the dislocation mechanism of the stationary stage of creep due to viscous motion of dislocations.

The minimum creep rate determined in the article should not be interpreted as a stationary creep rate, at which there is a dynamic equilibrium between strain hardening and thermal softening (constant dislocation substructure).

During high-temperature creep of MoSiBTiC molybdenum alloys, formation and growth of defor-

Table 6. Comparative heat-resistant properties of Ni, Nb, and Mo alloys

No.	Grade of alloy	Alloying system	Structure	Density, g/cm ³	T_{melt} , °C	Long-term strength σ_{τ}^T , MPa, where T is temperature, °C; τ is time, h
1	VZhM-4	Ni–Al–Cr–Mo–W–Ta–Co–Re–Ru	Single crystal	8.9	1370	$\sigma_{100}^{1100} = 170$; $\sigma_{100}^{1200} = 120$; $\sigma_{100}^{1200} = 55$
2	BKHA-1B	Ni–Al–Cr–Mo–W–Ti	Single crystal	7.94	≈ 1370	$\sigma_{100}^{1200} = 55$
3	Nb–Si	Nb–Si–Hf–Al–Cr–Mo–Ti	Directed	7.5	1750	$\sigma_{68}^{100} = 100$
4	Mo–Si	Mo–Si–B–TiC	Equiaxial	8.8–8.9	1900	$\sigma_{750}^{1350} = 170$; $\sigma_{400}^{1400} = 137$; $\sigma_{100}^{1100} = 400$

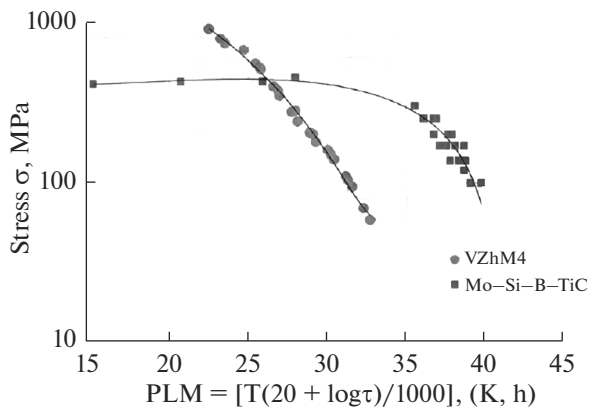


Fig. 9. Larsen–Miller curves of NHRA VZhM-4 monocystals and molybdenum alloy 65Mo–5Si–10B–10TiC of I generation.

mation pores, which are the source of nucleation of microcracks and their subsequent consolidation into a main crack, were found. In this article, an unusual experimental result was obtained, which consists in the fact that the long-term ductility of molybdenum alloys increases with a decrease in the applied stress, while it can reach 70%, as follows from Fig. 10. As a rule, an inverse relationship takes place in cast nickel heat-resistant alloys: long-term ductility increases with growth of stress.

As for the atomic mechanisms of creep and fracture of molybdenum alloys at ultrahigh temperatures of 1300–1600°C, presently there are no sufficiently convincing experimental data confirming a particular proposed mechanism. The authors of article [56] propose two mechanisms of creep of molybdenum alloys. Since formation of porosity is observed, it is reasonable to assume that grain-boundary diffusion plays a

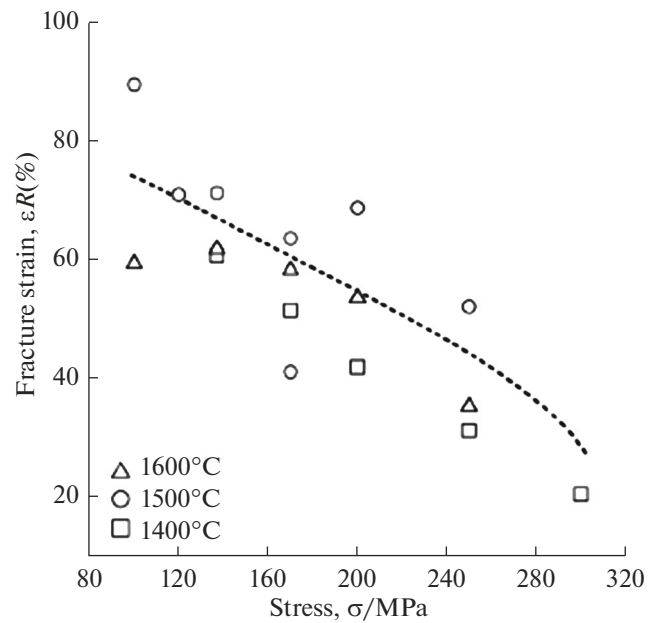


Fig. 10. The influence of the applied stress on creep fracture strain.

role in the ultra-high-temperature creep of the MoSiBTiC alloy; however, the power exponent $n = 3$ indicates that creep occurs not only according to Coble mechanism. The high values of long-term plasticity can be explained by interfacial slip along the Mo/T₂ and Mo/(Ti, Mo)C interfaces as well as by the dynamic return and recrystallization of molybdenum.

FRACTURE VISCOSITY

Analysis of short-term mechanical properties implies that molybdenum alloys MoSiBTiC are brittle

Table 7. Values of exponent n and activation energy Q of creep of molybdenum alloys Mo–Si–B*

No.	Year	Alloy	Type of test	Temperature, °C	Exponent, n	Q , kJ/mol
1	1979	Mo	Stretching	2000–2500	–	214
2	2001	Mo–9.4Si–13.8B	**	1400–1450	2.8	740
3	2007	Mo	**	1340–1540	5.0	234–246
4	2007	Mo–8.9Si–7.7B	Compression	1050–1315	2.0	444
5	2010	Mo–3Si–1.3B	Stretching	1000–1300	5.5	360
6	2014	Mo–9Si–8B–2Zr Mo–9Si–8B–4Zr	Stretching	1100–1250	3.0	560 460
7	2014	Mo–12.5Si–8.5B–27.5Ti Mo–9Si–8B–29Ti	Compression	1200–1300	3–4	560 384
8	2014	Mo–17.5 Si–8B	Compression	1093–1400	3.4–4.4	391
9	2016	Mo–17.5Si–10B	Compression	1093–1400	3–4.5	318
10	1979	Mo	Self-diffusion	1087–2500	–	460

* References to literature sources can be found in article [50].

** Constant strain rate tensile tests.

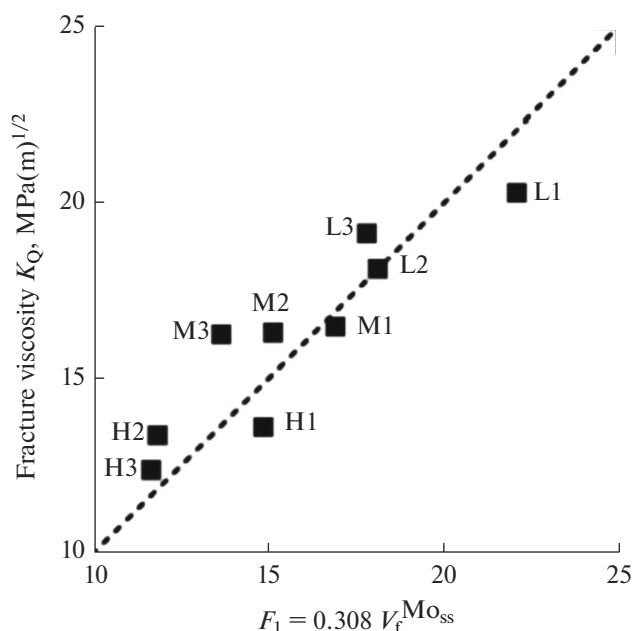


Fig. 11. Dependence of coefficient of fracture viscosity K_Q at 20°C on volume fraction of molybdenum.

up to a temperature of 1100°C. For the analysis of the mechanical properties of brittle alloys, an important engineering characteristic is crack resistance or fracture resistance. In the review article “Mo–Si–B Alloys for Ultra-High Temperature Structural Application” by Lemberg and Ritchie [10], a table is given in which more than 50 values of fracture toughness parameters are listed for alloys of the system Mo–Si–B, tested by three- or four-point bending or stretching of compact specimens with chevron notches. The values of the parameter K_Q vary within a wide range from 4.1 to 35 MPa m^{1/2} in the temperature range of 25–

1400°C. This indicates a significant dependence of the parameter K_Q on numerous factors such as the chemical and phase composition of alloys, their production technology, heat treatment, shape and geometric dimensions of samples and notches, test methods, and computation techniques.

A team of Japanese authors led by Professor Kiyosuki Yoshimi investigated the effect of microstructure on fracture resistance at room temperature of MoSiB alloys additionally doped with titanium carbides TiC or zirconium carbides ZrC [57, 58]. Alloys of three dissimilar compositions with different content of phase components (α Mo, T_2 phases, titanium and zirconium carbides) were obtained by the standard VAM method followed by annealing at 1800°C for 24 h. The tests were carried out by the method of four- or three-point bending of specimens with chevron cut. The fracture resistance was computed either by standard methods according to ASTM C1421-10 or by the Irwin criterion. For the alloy doped with titanium carbide TiC, the maximum value of fracture resistance according to Irwin was $K_Q = 15.2$ MPa m^{1/2}, and for the alloy doped with zirconium carbide, $K_Q = 20.3$ MPa m^{1/2}. The results of these articles allowed making the following conclusions. Firstly, the fracture resistance at room temperature increases in proportion to the increase in the volume fraction of plastic molybdenum in the alloy, as can be seen in Fig. 11. On the contrary, a high volumetric content of the brittle T_2 phase in the alloy causes a decrease in K_Q .

Secondly, the nature of the topological connectivity of phases is of great importance. Solid solution α Mo increases the fracture resistance K_Q if it is a topologically simply connected matrix, as shown in Fig. 12a, where particles of the brittle hardening T_2 phase are dispersed in a plastic solid solution of molybdenum. Otherwise, when the brittle T_2 phase is a simply connected

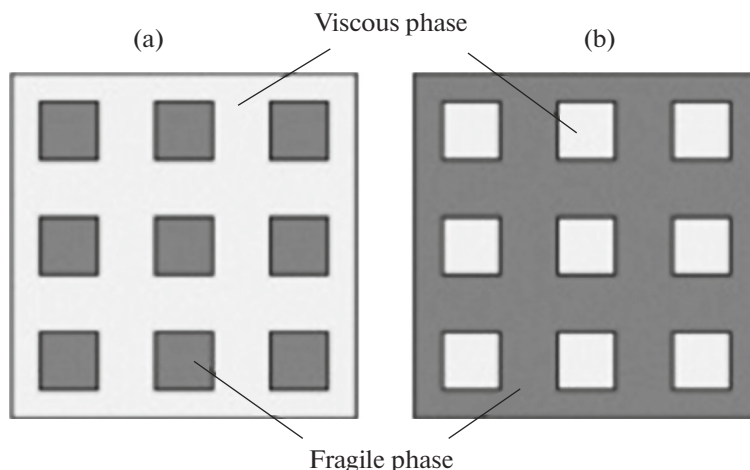


Fig. 12. Structure diagram of alloy Mo–Si–B–TiC: (a) plastic α Mo, in which fragile T_2 phase is dispersed; (b) fragile T_2 phase, in which particles of α Mo are dispersed.

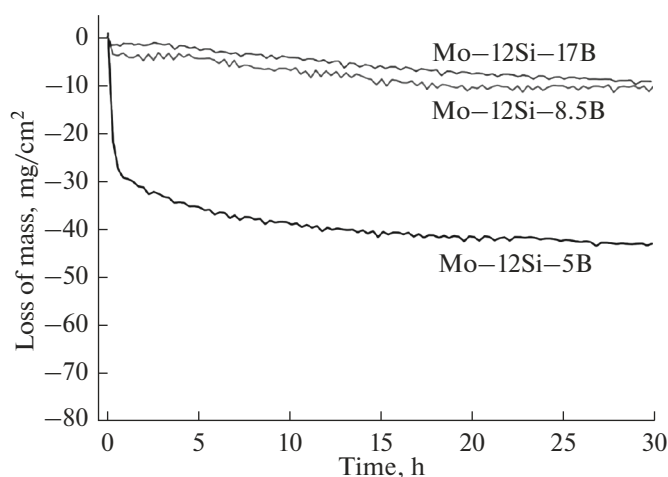


Fig. 13. Kinetic curves of oxidation of alloys Mo-12Si-xB at temperature of 1000°C.

matrix in which plastic particles of α Mo are dispersed (see Fig. 12b), the latter does not have a positive effect on the increase in fracture resistance.

Various mechanisms of the influence of titanium and zirconium carbides on fracture processes are considered, in particular, stopping of microcracks, branching of cracks, and delamination of interphase surfaces [59, 60].

A similar character of crack resistance was observed by the authors of [61, 62] in composite materials based on the Si-B-C-Mo system consisting of alternating layers of high-temperature ceramic compounds and molybdenum obtained by spark plasma sintering.

OXIDATION RESISTANCE OF ALLOYS Mo-Si-B-TiC

Oxidation resistance is one of the most important properties of structural alloys designed for high temperature service. Oxidation of molybdenum begins at temperature of about 300°C, and at temperatures above 700°C, oxidation occurs with formation of volatile oxide MoO₃ in the form of white smoke and proceeds so quickly that the practical use of molybdenum products under conditions of increased temperature is impossible without protective coatings [63, 64]. Commercial alloys have nearly the same low oxidation resistance as pure molybdenum.

The increase in oxidation resistance of molybdenum alloys is carried out by methods well known in materials science, namely, by macroalloying with such elements as Ti, B, Cr, and Zr, by microalloying mainly with rare earth elements (REM), and by creating and applying protective coatings.

First, let us consider the effect of macroalloying on heat resistance of MoSiB molybdenum alloys. To increase the resistance to oxidation, boron doping is

used, which together with Si contributes to the formation of a protective glassy layer. The effect of boron content on the oxidation resistance of Mo-Si-xB alloys, where $x = 5, 8.5, 17$ at % (Fig. 13), was investigated in [65]. The alloy with the lowest boron content had the greatest weight loss at the initial stage of oxidation. Studies of the microstructure together with the analysis of oxidation curves showed that, at high boron content, the viscosity of borosilicate scale significantly decreases, and at the stage of stable oxidation, a continuous protective glassy coating is formed. It is known that addition of La₂O₃ particles to the alloy has a positive effect on resistance to oxidation. In this case, lanthanum oxides act as a blocking phase and can prevent penetration of gas bubbles of MoO₃ oxide through the glass silicate layer.

The first generation MoSiBTiC alloys possess high mechanical properties, but have low resistance to oxidation owing to the low silicon concentration of ≈ 5 at%. Therefore, modernization of this alloy primarily consisted in increasing the heat resistance without deteriorating the mechanical properties. This was done, firstly, by optimizing the chemical and phase composition of the alloy and, secondly, by alloying with chromium to improve the heat resistance at medium temperatures.

Obviously, in order to increase the heat resistance, it is necessary to decrease the Mo content and to increase the concentrations of silicon and titanium. In [66, 67], an alloy of the composition 38Mo-17Si-5B-20Ti-10TiC was investigated, in which the concentration of Ti was increased, and therefore it contained a new phase Ti₅Si₃ along with silicides Mo₅SiB₂ and Mo₃Si as well as TiC carbides. The authors studied the nature of oxidation at 1100 and 1300°C in an atmosphere of a mixture of oxygen and argon gases at the partial pressure ratio $p_{O_2}/p_{Ar} = 0.25$. Under these conditions, the formed oxide layer consisted of crys-

talline TiO_2 and amorphous SiO_2 . Microstructure studies showed that T_2 and Ti_5Si_3 interlayers serve as barriers to the oxidation process. It was found that the oxidation resistance is improved by applying high-temperature deformation. Figure 14 shows curves of oxidation at 1100 and 1300°C of thermally treated samples before and after deformation.

An increase in heat resistance is facilitated by alloying alloys with zirconium borides ZrB_2 , which are widely used in ceramic composites SiC to increase oxidation resistance, increasing the stability and resistance of the glassy SiO_2 layer. Studies [68] showed that the fluidity of borosilicate glass is controlled by the presence of zirconium boride ZrB_2 . At the initial stage of oxidation, zirconium boride promotes rapid spreading of the SiO_2 oxide layer over the entire surface and subsequent passivation at the next stage. Zirconium, as the most important glass-forming element, improves the passivation of vitreous scale and reduces the oxygen diffusion coefficient by increasing the viscosity.

The results of a detailed study of the effect of 2 at % zirconium on the microstructure, hardness, and isothermal and nonisothermal heat resistance of alloys 76Mo–14Si–10B (at %) and 79.5Mo–12Si–8.5B (at %) obtained by arc melting and spark plasma sintering are presented in article [69]. The alloys contained three phases: Mo, Mo_5SiB_2 , and Mo_3Si ; and as a result of the refining action of zirconium, dispersed particles of the ZrO_2 phase were found in the structure. In the course of isothermal oxidation in the temperature range of 800–1300°C, a sharp initial decrease in the mass of the samples due to the evaporation of volatile oxides of MoO_3 was found. Oxides $\text{B}_2\text{O}_3 + \text{SiO}_2$, MoO_2 , and Mo were found in the scale of all alloys, and zirconium oxides ZrO_2 , ZrSiO_4 , and $\text{Zr}(\text{MoO}_4)_2$ were additionally found in Zr-containing alloys. The greatest decrease in weight loss of the samples is observed during oxidation of Zr-containing alloys at 800°C owing to transformation of MoO_3 into the non-volatile $\text{Zr}(\text{MoO}_4)_2$ phase.

Alloying with tungsten favorably affects the oxidation resistance of MoSiB alloys in the temperature range of 1000–1300°C, and the effectiveness of the impact increases with growth of temperature [70]. It was found that, in the uncoated alloy, a significant weight loss was observed upon exposure at 1000°C, which was associated with the presence of WO_3 oxide, which destroys the borosilicate layer. However, at 1300°C, nonvolatile oxide WO_2 promotes formation of a continuous borosilicate layer. Low resistance to oxidation at lower temperatures was associated with unfavorable oxidation of Mo and W in combination with slow growth of the borosilicate layer.

The increase in high-temperature heat resistance by changing the chemical and phase composition of MoSiB alloys has a limited scope. A more radical way

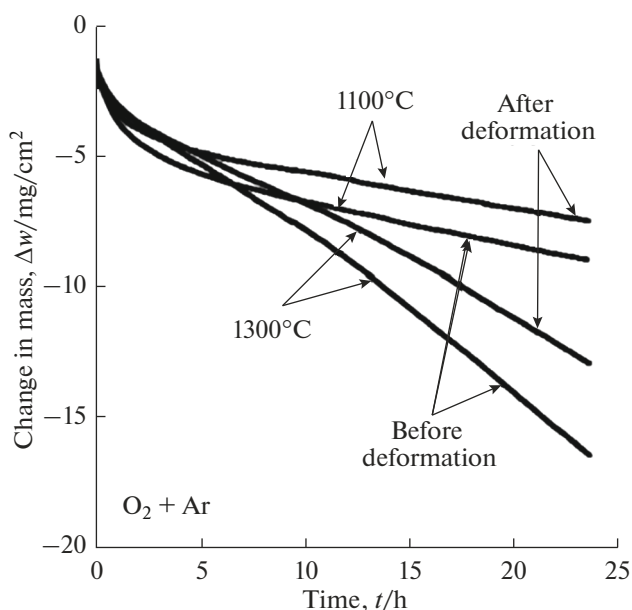


Fig. 14. Curves of oxidation at 1100 and 1300°C of thermally processed samples before and after deformation.

is to develop compositions and methods for applying protective coatings to form a boron silicate layer.

There is extensive literature devoted to the development of protective coatings and methods of their application to molybdenum and its alloys. The review article “Silicide Coatings on Molybdenum: Preparation, Structure, Properties” [71] describes the current state of research on the structure and properties of silicide coatings, as well as methods of their formation, including diffusion siliciding of molybdenum from powder media. This article analyzes the latest articles related to the study of heat resistance of molybdenum alloys of the Mo–Si–B and Mo–Si–B–TiC systems, as well as silicide protective coatings in oxidizing environments and their ability to passivate the surface owing to the formation of oxide films. The quality of this film, its continuity, density, low oxygen diffusion coefficient, and self-healing ability determine the protective properties of silicide coatings.

The method of applying such coatings is also essential. When forming silicide coatings on high-melting metals, thermochemical methods are most often used, among which gas-phase siliciding can be distinguished.

On Mo–3Si–1B alloys, protective coatings are applied by batch cementation—chemical gas deposition using powder mixtures of various compositions. For example, in [72], powder mixtures of the following composition are used: 35Si–1B (wt %) or 20Si–1B (wt %), filler powder Al_2O_3 , halogen activator NaF or NH_4Cl . Sometimes a layer of pure molybdenum is preliminarily applied to the surface of the alloy. Batch cementation (Si–B) is carried out in corundum tubu-

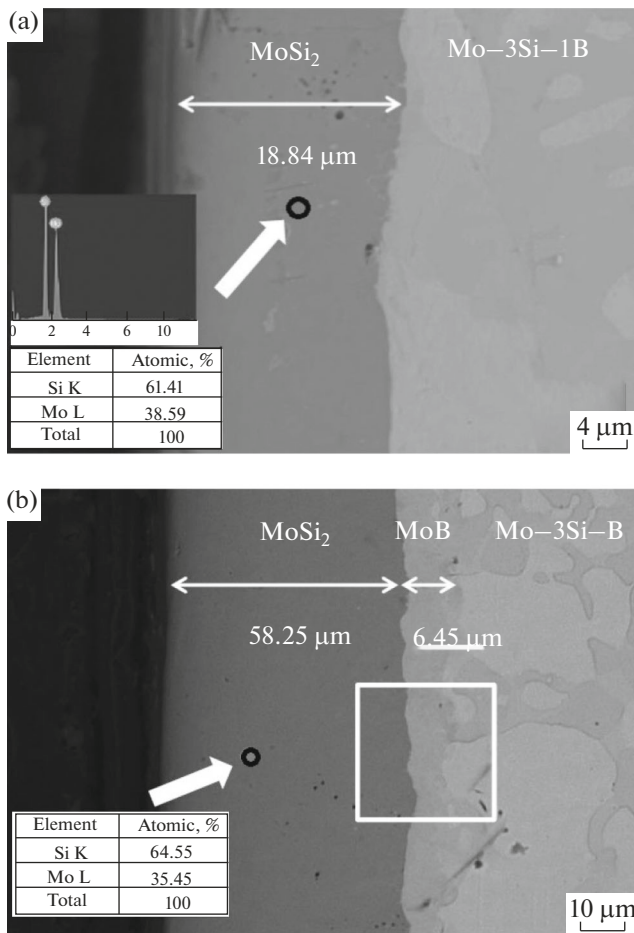


Fig. 15. Microstructure of the coating on substrate of Mo-3Si-1B after pack cementation: (a) 1000°C for 12 h; (b) 1100°C for 48 h [73].

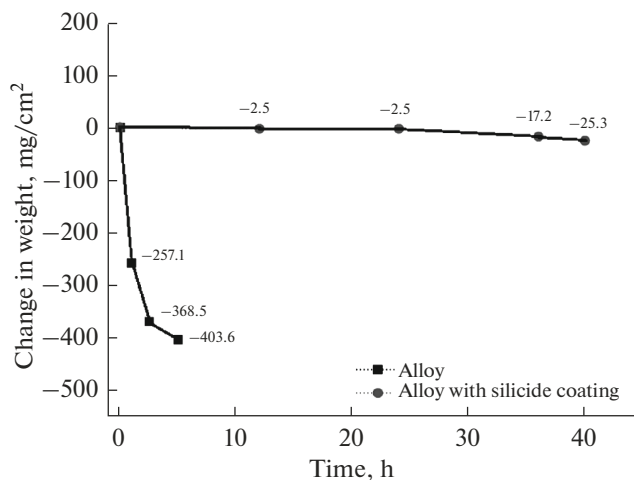


Fig. 16. Change in mass of alloy samples with coating and without it during isothermal oxidation at temperature of 1400°C [73].

lar furnaces at temperature of 1000–1100°C for 12–48 h in an argon atmosphere. After cementation, annealing is carried out in the temperature range of 1200–

1400°C for 30–10 h to form the required coating microstructure. Aluminoborosilicate coatings applied by batch cementation to the surface of Mo-3Si-1B alloys protect not only from high-temperature oxidation but also from the effects of water vapor, hot corrosion, and thermocyclic oxidation, as well as from the effects of surface fluxes.

A series of articles by South Korean authors is devoted to the study of oxidation kinetics of Mo-3Si-1B alloys with protective coatings obtained by batch cementation with other compositions of powder mixtures [73–75]. Batch cementation of the Mo-3Si-1B alloy was carried out in a mixture of powders of the following composition, wt %: 30 Si; 65 Al₂O₃; 5 activator NaF [73].

Figure 15 shows the microstructure of the coating after alloy cementation in two modes: 1000°C for 12 h and 1100°C for 48 h. In the first mode, the outer layer of molybdenum disilicide MoSi₂ has a thickness of ≈18 μm. In the second mode, this layer grows to ≈58 μm, then an interlayer of molybdenum boride MW with a thickness of 6.5 μm is formed, and next the substrate of the Mo-3Si-1B alloy follows.

Kinetic curves of isothermal oxidation of the Mo-3Si-1B alloy with the deposited coating according to the second regime and the alloy without the coating are shown in Fig. 16. The protective effect of the coating is clearly manifested in the oxidation process at temperature of 1400°C for 40 h, mainly owing to the presence of an intermediate MoB layer between the surface layer of MoSi₂ and the substrate.

It is important to note the self-healing property of silicide protective coatings on molybdenum alloys of the Mo-Si-B system at high temperatures. Owing to the peculiarities of the transformation characteristics in the Mo-Si-B system, cracks and scratches on the outer MoSi₂ layer can self-heal by B atoms from the MoB sublayer, leading to the restoration of the characteristics. Self-healing methods for microcracks in matrices are widely used in polymer composite materials in order to increase resistance to shock loads and crack resistance [73].

The same group of authors investigated the heat resistance at temperatures of 800 and 1300°C of this alloy with coatings obtained by batch cementation (Si + Al) of other powder compositions: 10Si-10Al-5NH₄F-75Al₂O₃ (wt %) [74] and 25Al-70Al₂O₃-5NH₄Cl (wt %) [76]. Figure 17 shows kinetic curves of oxidation at the indicated temperatures.

As can be seen, the mass of uncoated specimens sharply decreased by ≈62% after oxidation at 1300°C in 5 h, while the mass of specimens with a coating after oxidation at 800 and 1300°C for 48 h of testing hardly changed; it even slightly increased owing to the formation of a surface film of Al₂O₃, which prevented the evaporation of the volatile oxide MoO₃.

Figure 18 shows a diagram of the structure of protective coatings obtained by batch cementation (Si + Al)

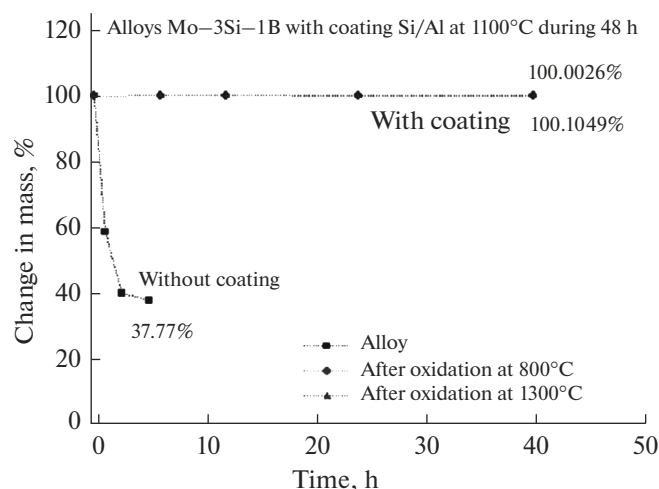


Fig. 17. Change in mass of samples of alloy Mo-3Si-1B with coating and without it during isothermal oxidation at temperatures of 800 and 1300°C [75].

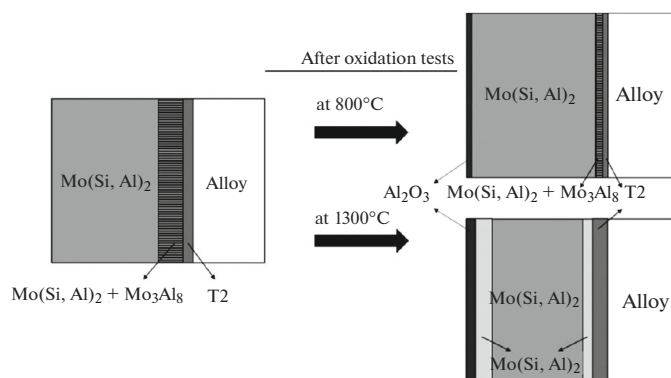


Fig. 18. Diagram of the formation of the structure of protective coatings obtained by batch cementation (Si + Al) after oxidation of alloy at 800 and 1300°C [75].

before and after oxidation of the alloy at 800 and 1300°C.

In the protective coating obtained by batch cementation (Si + Al), the aluminum-rich Mo_3Al_8 phase was formed in the two-phase layer and the protective $\text{Mo}(\text{Si}, \text{Al})_2$ layer was formed on the outer surface. In an oxidizing atmosphere at 800 and 1300°C, the rate of diffusion of Al atoms will be higher than that of Si atoms and therefore heat-resistant oxide Al_2O_3 will be formed on the surface. As noted earlier, after batch cementing (Si + B), the heat-resistant oxide of molybdenum disilicide MoSi_2 is formed on the outer surface of the protective coating of the same Mo-3Si-1B alloy (see Fig. 15).

CONCLUSIONS

Comparative analysis of level of properties of heat-resistant molybdenum alloys MoSiBTiC and single

crystals of nickel heat-resistant alloys of the latest generations allows us to make the following conclusions.

The alloying complex of molybdenum alloys is more economical in comparison with nickel alloys for casting monocrystalline blades and does not contain heavy and expensive elements such as rhenium and ruthenium. In terms of density, these alloys do not differ. The solidus temperature of MoSiBTiC alloys is equal to $\approx 2000^\circ\text{C}$ and is 650°C higher than that of the cast NHRA.

Heat-resistant nickel alloys are melted in vacuum induction furnaces and single-crystal blades are produced by precision casting in directional crystallization units. MoSiBTiC alloys with polycrystalline structure are made by VAM or powder metallurgy methods.

Young's modulus E of MoSiBTiC alloys varies within 325–270 GPa in the temperature range of 24–1200°C, which significantly exceeds the change in

Young's modulus of 140–90 GPa of single crystals of nickel alloys in [001] orientation at the same temperatures.

Table 5 and Fig. 8b imply that the tensile strength of samples of molybdenum alloy of composition Mo–8.9Si–7.7B is significantly inferior to the strength of single crystals [001] of NHRA up to temperature of 1150°C, and above this temperature, the dependence is inverse. These data refer to the ternary system. It can be assumed that carbide hardening will slightly increase the strength of MoSiBTiC alloys, but the quality ratio will remain the same. Up to the brittle–ductile transition temperature, molybdenum alloy does not exhibit ductility. It is pertinent to note that a similar temperature dependence of strength is observed upon in situ tension of Nb–Si composites: up to 1150°C, NHRA single crystals are much stronger than composites, and in the range 1150–1400°C, composites are two times stronger than single crystals [77].

According to some estimates [78], the fracture resistance of materials for static parts of gas turbine engines should be at least 15 MPa m^{1/2}, and for rotor parts, at least 20 MPa m^{1/2}. The data given in the article for the molybdenum alloy MoSiBTiC fit into this interval $K_q = 15\text{--}20 \text{ MPa m}^{1/2}$.

As for 100-hour long-term strength of MoSiBTiC alloys, at temperature of 1100°C, it is equal to $\sigma_{100}^{1100} = 400 \text{ MPa}$ and is more than two times higher than the high-temperature strength of single crystals of NHRA $\sigma_{100}^{1100} = 170 \text{ MPa}$. At higher temperatures, the advantage of MoSiBTiC alloys is even greater. However, at temperatures below 950–1000°C, MoSiBTiC molybdenum alloys are inferior to NHRA single crystals in long-term and short-term strength.

Long-term performance of molybdenum heat-resistant alloys in oxidizing environments at increased temperatures is possible only when creating and using protective coatings. For molybdenum alloys, coatings must operate not only at temperatures above 1200°C but also at average temperatures of $\approx 800^\circ\text{C}$. The currently developed methods of batch cementing make it possible to apply aluminoborosilicate coatings, which are able to protect MoSiBTiC alloys from oxidation at temperatures of 800 and 1300°C for up to 50 h. A feature of such coatings is the ability to self-heal emerging microcracks and restore protective characteristics.

ACKNOWLEDGMENTS

We are grateful to E.N. Sheftel and N.V. Petrushina for valuable remarks after reading the manuscript.

REFERENCES

1. Kablov, E.N., Ospennikova, O.G., and Svetlov, I.L., Highly efficient cooling of GTE hot section blades, *Aviats. Mater. Tekhnol.*, 2017, no. 2 (47), pp. 3–14. <https://doi.org/10.18577/2071-9140-2017-0-2-3-14>
2. Kablov, E.N., Svetlov, I.L., and Efimochkin, I.Yu., High-temperature Nb–Si composites, *Vestn. Mosk. Gos. Tekh. Univ. im. N.E. Bauman, Ser. Mashinost.*, 2011, no. S2, pp. 164–173.
3. Kablov, E.N., Bondarenko, Yu.A., and Echin, A.B., Development of technology of cast superalloys directional solidification with variable controlled temperature gradient, *Aviats. Mater. Tekhnol.*, 2017, no. S, pp. 24–38. <https://doi.org/10.18577/2071-9140-2017-0-S-24-38>
4. Svetlov, I.L., Kuzmina, N.A., Zavodov, A.V., and Zaitsev, D.V., Thermal stability of interfaces between the niobium matrix and $\gamma\text{-Nb}_5\text{Si}_3$ silicide in eutectic Nb–Si composites, *Tr. Vseross. Inst. Aviats. Mater.*, 2018, no. 8 (68), pp. 28–37. <https://doi.org/10.18577/2307-6046-2018-0-8-28-37>. <http://www.viam-works.ru> (Accessed November 26, 2019).
5. *Beyond Nickel-Based Superalloys I*, Bavaria, Germany, 2013.
6. *Beyond Nickel-Based Superalloys II*, Cambridge, GB, 2016.
7. *Beyond Nickel-Based Superalloys III*, Nara, Japan, 2019.
8. Svetlov, I.L., High-temperature Nb–Si composites. Part 1, *Inorg. Mater.: Appl. Res.*, 2011, vol. 2, art. ID 307. <https://doi.org/10.1134/S2075113311040125> Svetlov, I.L., High-temperature Nb–Si composites. Part 2, *Inorg. Mater.: Appl. Res.*, 2011, vol. 2, art. ID 316. <https://doi.org/10.1134/S2075113311040125>
9. Karpov, M.I., Niobium-base refractory alloys with silicide and carbide hardening current status and prospects, *Met. Sci. Heat Treat.*, 2018, vol. 60, nos. 1–2, pp. 7–12.
10. Lemberg, J.A. and Ritchie, R.O., Mo–Si–B alloys for ultra high temperature structural application, *Adv. Mater.*, 2012, vol. 24, pp. 3445–3480.
11. Choi, W.J., Park, C.W., Park, J.H., Kim, Y.D., and Byun, J.M., Research trends of the Mo–Si–B alloys as next generation ultra-high temperature alloys, *J. Korean Powder Metall. Inst.*, 2019, vol. 26, no. 2, pp. 156–165.
12. Kablov, E.N., Innovations of VIAM as part of implementing the Strategic Directions of Development of Materials and Technologies of Their Processing for the Period up to 2030, *Aviats. Mater. Tekhnol.*, 2015, no. 1 (34), pp. 3–33. <https://doi.org/10.18577/2071-9140-2015-0-1-3-33>
13. Novotny, H., Dimakopoulous, E., and Kudielka, H., Untersuchungen in den dreistoffsystemen: Molibden–silizium–bor, wolfram–silizium–bor in dem system: $\text{VSi}_2\text{–TaSi}_2$, *Monatsch. Chem.*, 1957, no. 88, pp. 180–192.
14. Yang, Y. and Chang, Y.A., Thermodynamic modeling of the Mo–Si–B system, *Intermetallics*, 2005, no. 13, pp. 121–128.
15. Berczik, D.M., US Patent 5595616, 1997.
16. Berczik, D.M., US Patent 5683156, 1997.
17. Ha, S.-H., Yoshimi, K., Nakamura, J., Kaneco, T., Maruyama, K., Tu, R., and Goto, T., Experimental study of Moss–T₂, Moss–Mo₃Si–T₂, Mo₃Si–T₂ eutec-

- tic reaction in Mo rich Mo–Si–B alloys, *J. Alloys Compd.*, 2014, no. 594, pp. 52–59.
18. Hasemann, G., Kruger, M., Palm, M., and Stein, F., Microstructure of ternary Eutectic refractory Me–Si–B (Me = Mo, V) alloy systems, *Mater. Sci. Forum*, 2018, vol. 941, pp. 827–832.
 19. Hasemann, G., Kaplunenko, D., Bogomol, I., and Kruger, M., Near-eutectic ternary Mo–Si–B alloys: Microstructures and creep properties, *JOM*, 2016, vol. 68, no. 11, pp. 2847–2853.
 20. Ha, S.-H., Yoshimi, K., Maruyama, K., Tu, R., and Goto, T., Phase formation and solidification routes near Mo–Mo₅SiB₂ eutectic point in Mo–Si–B system, *Mater. Trans.*, 2010, vol. 51, no. 9, pp. 1699–1704.
 21. Hasemann, G., Ida, S., Zhu, L., Lisawa, T., Yoshimi, K., and Krüger, M., Experimental assessment of the microstructure evolution and liquidus projection in the Mo-rich Mo–Si–B system, *Mater. Des.*, 2020, vol. 185, art. ID 108233.
<https://doi.org/10.1016/j.matdes.2019.108233>
 22. Miyamoto, S., Yoshimi, K., Ha, S.-H., Kaneco, T., Nakamura, J., Tu, R., and Goto, T., Phase equilibria, microstructure, and high-temperature strength of TiC-added Mo–Si–B alloys, *Metall. Mater. Trans. A*, 2014, vol. 45, pp. 1112–1123.
 23. Fukuyama, H., Sawada, R., Nakashima, H., Ohtsuka, M., and Yoshimi, K., Study solidification pathway of MoSiBTiC alloy by optical thermal analysis and in situ observation with electromagnetic levitation, *Sci. Rep.*, 2019, vol. 9, art. ID 15049.
 24. Eremenko, V.N., Velikanova, T.Ya., and Artyukh, L.V., *Troinye sistemy molibdena s uglerodom i perekhodnymi metallami IV gruppy* (Triple Systems of Molybdenum with Carbon and Transition Metals of Group IV), Kiev: Naukova Dumka, 1985.
 25. Litovchenko, S.V., Petrichenko, A.P., Beresnev, V.M., Kiper, I.G., and Vitkovskii, E.A., Behavior of molybdenum-silicide coating composites under mechanical and thermal loads, *Fiz. Inzh. Poverkhnost.*, 2011, vol. 9, no. 1, pp. 87–93.
 26. Yokoyama, Y. and Inoue, A., Cast of bulk glassy alloys, *J. Soc. Mater. Sci. Jpn.*, 2009, vol. 58, no. 3, pp. 193–198.
 27. Yoshimi, K., Tsurekawa, S., Fukuyama, H., and Sato, Y.S., Mechanical properties and high-temperature applications of MoSiBTiC alloys, *Proc. Intermetallics Conf., Bad Staffelstein, Germany, 2017*, art. ID O-IT 01-13.
 28. Bewlay, B.P. and Dalpe, D.J., US Patent 6059015, 2000.
 29. Koizumi, Y., Zhu, C., Yamazaki, T., Chiba, A., Yuge, K., Kishida, K., and Inui, H., Phase field simulation of spontaneous C11_b–MoSi₂–Mo₅Si₃ eutectic reaction in directional solidification, *Proc. Fall Meeting & Exhibit, Boston, Massachusetts, November 25–30, 2018*, PM 06.02.08.
 30. Hasseman, G., Kaplunenko, D., Bogomol, I., and Kruger, M., Near-eutectic ternary Mo–Si–B alloys: Microstructures and properties, *JOM*, 2016, vol. 68, no. 11, pp. 2847–2853.
 31. Jehanno, P., Heilmaier, M., and Kester, Y., Characterization of an industrially processed Mo-based silicide alloy, *Intermetallics*, 2004, vol. 12, nos. 7–9, pp. 1005–1009.
 32. Kruger, M., Kauss, O., Naumenko, K., Burmeister, C., Wessel, E., and Schmelzer, J., The potential mechanical alloying to improve the strength and ductility of Mo–9Si–8B–1Zr alloys – experiments and simulation, *Intermetallics*, 2019, vol. 113, art. ID 106558.
 33. Li, R., Zhang, G., Li, B., Chen, X., Ren, S., Wang, J., and Sun, J., The multi-scale microstructure and strengthening mechanisms of Mo–12Si–5B times Zr (at %) alloys, *Int. J. Refract. Met. Hard Mater.*, 2017, vol. 68, pp. 65–74.
 34. Lin, X.-H., Li, B., Ping, L., Liang, J., Gao, X.-Q., and Zhang, X., Microstructure and improved mechanical properties of Mo–12Si–8.5B alloys with lanthanum oxide addition, *Rare Met.* 2019, vol. 38, no. 9, pp. 848–854.
 35. Bol'shakova, A.N., Efimochkin, I.Yu., and Murasheva, V.V., Metallographic study of high-temperature composite materials based on Mo–Si–B alloys, *Vopr. Materialoved.*, 2014, no. 3 (79), pp. 41–46.
 36. Bol'shakova, A.N., Efimochkin, I.Yu., and Bobrovskii, A.P., Studies of the microstructure and physical and mechanical properties of layered metal composite materials based on a molybdenum matrix, *Inorg. Mater.: Appl. Res.*, 2018, vol. 9, pp. 197–200.
<https://doi.org/10.1134/S2075113318020077>
 37. Chen, L., Wei, R., Tang, K., Li, R., Jiang, F., and San, J., Effect of doping nano-La₂O₃ on the microstructure and mechanical properties of Mo–9Si–18B alloys, *Mater. Trans.*, 2018, vol. 59, no. 5, pp. 764–770.
 38. Li, W., Ai, T., Dong, H., and Zhang, G., Tribological properties of Mo–Si–B alloys doped with La₂O₃ and tested at 293–1173 K, *Materials (Basel)*, 2019, vol. 12, no. 12, pp. 2–13.
 39. Li, B., Lin, X., Zhang, G., Li, L., and Zhang, P., Optimization of multi-phase Mo–12Si–8.5B alloy by SiC whisker, *JOM*, 2018, vol. 70, no. 11, pp. 2529–2535.
 40. Zhou, W., Sun, X., Tsunodo, K., Kikuchi, K., Nomura, N., Yoshimi, K., and Kawasaki, A., Power fabrication and laser additive manufacturing of MoSiBTiC alloy, *Intermetallics*, 2019, vol. 104, pp. 33–42.
 41. Schmelzer, J., Rittinghaus, S.-K., Weisheit, A., Stobic, M., Paulus, J., Gruber, K., Wessel, E., Kruger, M., and Heibze, C., Printability of Mo–Si–B alloys via additive manufacturing, *Proc. Fall Meeting & Exhibit, Boston, Massachusetts, November 25–30, 2018*, PM 06.02.05.
 42. Schmelzer, J., Rittighaus, S.K., Weishelt, A., Stobic, M., Paulus, J., Gruber, K., Wessel, E., Heinze, C., and Kruger, M., Printability of gas atomized Mo–Si–B powders by laser metal deposition, *Int. J. Refract. Met. Hard Mater.*, 2019, vol. 78, pp. 123–126.
 43. Sun, X., Kikuchi, K., Nomura, N., Yoshimi, K., and Kawasari, A., In-situ synthesized TiC/Mo-based composites via laser bed fusion, *Mater. Des.*, 2018, vol. 146, pp. 116–124.
 44. Makineni, S.K., Kini, A.R., Jagle, A.E., Springer, N., Raabe, D., and Gault, B., Synthesis and Stabilization of a new Phase regime in a Mo–Si–B based alloy by laser – based additive manufacturing, *Acta Mater.*, 2018, vol. 151, pp. 31–60.
 45. Uemura, S., Yamanuro, T., Kim, J.W., Morisono, Y., Tsurekawa, S., and Yoshimi, K., Quantitative evaluation of microstructure in Mo–Si–B–TiC alloy pro-

- duced by melting and tilt casting method, *Mater. Trans.*, 2018, vol. 59, no. 1, pp. 136–145.
46. Hatakeyama, T. and Yoshimi, K., Oxidation resistance and high-temperature strength of Cr-added novel MoSiBTiC alloy, *Proc. Fall Meeting & Exhibit (Boston, Massachusetts, November 25–30, 2018)*, PM 06.05.
 47. Nakamura, J., Kanekon, D., and Yoshimi, K., Characterization of Mo/Mo₂C interface in MoSiBTiC alloy, *Mater. Lett.*, 2016, vol. 180, pp. 340–343.
 48. Biragoni, P.G. and Heilmaier, M., FEM-Simulation of real and artificial microstructures of Mo–Si–B alloys for elastic properties and comparison with analytical methods, *Adv. Eng. Mater.*, 2007, vol. 10, no. 9, pp. 882–887.
 49. Jehanno, P., Heilmaier, M., Kestler, H., Böning, M., Venskutonis, A., Belway, B., and Jackson, M., Assessment of a powder metallurgical processing route for refractory metal silicide alloys, *Metall. Mater. Trans. A*, 2005, vol. 36, pp. 515–523.
 50. Jehanno, P., Heilmaier, M., and Kester, Y., Characterization of an industrially processed Mo-based silicide alloy, *Intermetallics*, 2004, vol. 12, pp. 1005–1009.
 51. Kamata, S.Y., Kanecon, D., Lu, Y., Secido, N., Maruyama, K., Egeller, G., and Yoshimi, K., Ultra-high – temperature tensile creep of TiC-reinforced Mo–Si–B-based alloy, *Sci. Rep.*, 2018, vol. 8, art. ID 10487.
 52. Yoshimi, K., Yamamoto, S., Nakamura, J., and Maruyama, K., High temperature creep strength and room-temperature fracture toughness of MoSiBTiC alloys, *Beyond Nickel-Based Superalloys II*, Cambridge, UK, 2016.
 53. Kamata, S., Saito, T., Maruyama, K., and Yoshimi, K., Tensile creep resistance of 65Mo–5Si–10B 10TiC (at.%) alloy in range of 1400–1700°C, *Proc. Intermetallics*, Bad Staffelstein, Germany, 2017, poster P-17.
 54. Yoshimi, K., Tsurekawa, S., and Fukuyama, H., Mechanical properties and high temperature applications of MoSiBTiC alloys, *Proc. Intermetallics*, Bad Staffelstein, Germany, 2017, O-IT 03.
 55. Sizova, R.N., Bychkova, Zh.A., and Lysenko, A.I., Generalized curves of the long-term strength of the main alloys for the turbine blades and disks of the gas turbine engine, *Al'bom Tsent. Inst. Aviats. Motorostr.*, 1977, no. 8138.
 56. Yoshimi, K., Kamata, S.Y., Nakayama, S., Uemura, S., Tsurekawa, S., Egeler, G., and Maruyama, K., Role Mo solid solution on ultrahigh temperature tensile creep deformation MoSiBTiC alloy, *Proc. Fall Meeting & Exhibit, Boston, Massachusetts, November 25–30, 2018*, PM 06.02.02.
 57. Moriyama, T., Yoshimi, K., Zhao, M., Masnou, T., Yokoyama, T., Nakamura, J., Katsui, H., and Goto, T., Room temperature fracture toughness of MoSiBTiC alloys, *Intermetallics*, 2017, vol. 84, pp. 92–102.
 58. Nakayama, S., Sekido, N., Uemura, S., Tsurekawa, S., and Yoshimi, K., Effect of microstructural continuity on room-temperature fracture toughness of ZrC-Added Mo–Si–B alloys, *Mater. Trans.*, 2018, vol. 59, no. 4, pp. 518–527.
 59. Li, R., Li, B., Wang, T., Ren, S., Chen, X., Wang, J., and Zhang, G., Improved fracture toughness of a Mo–12Si–8.5B–3Zr alloy by grain coarsening and its multiple toughening mechanisms, *J. Alloys Compd.*, 2018, vol. 743, pp. 716–727.
 60. Wang, J., Li, B., Li, R., Chen, X., Chen, X., and Zhang, G., High toughness and strength of Mo–12Si–8.5B–Zr B₂ alloy resulting from a bimodal α Mo grain structure, *Int. J. Refract. Met. Hard Mater.*, 2020, vol. 86, art. ID 105129.
 61. Vaganova, M.L., Erasov, V.S., Sorokin, O.Yu., Efimochkin, I.Yu., and Kuznetsov, B.Yu., Studies of microstructure and properties of multi-layered high-temperature ceramics-refractory metal-based composite, *Perspekt. Mater.*, 2019, no. 9, pp. 15–23.
 62. Vaganova, M.L., Erasov, V.S., Sorokin, O.Yu., Kuznetsov, B.Yu., and Voronov, V.A., Crack-resistant composite materials with a multilayer structure based on refractory compounds, *Proc. 22nd Int. Sci. Technol. Conf. on Structures and Technologies for Manufacturing Articles from Non-Metallic Materials, Obninsk, Russia, October 15–17, 2019*.
 63. Morgunova, N.N., Klypin, B.A., Boyarshinov, V.A., Tarakanov, L.A., and Manegin, Yu.V., *Splavy molibdena (Molybdenum Alloys)*, Moscow: Metallurgiya, 1975.
 64. Perepezko, J.H. and Sakidja, R., Oxidation-resistant coatings for ultra-high-temperature refractory Mo-based alloys, *JOM*, 2010, vol. 62, no. 10, pp. 13–19.
 65. Li, R., Li, B., Chen, X., Wang, J., Wang, T., Gong, Y., Ren, S., and Zhang, G., Variation of phase composition of Mo–Si–B alloys included by boron and their mechanical properties and oxidation resistance, *Mater. Sci. Eng., A*, 2019, vol. 749, pp. 196–209.
 66. Zhao, M., Yoshimi, K., and Yokoyama, K., Oxidation behavior and mechanical properties of Ti-enriched MoSiBTiC alloy, in *Beyond Nickel-Based Superalloys II*, Cambridge, UK, 2016.
 67. Zhao, M., Nakayama, S., Hatakeyama, T., Nakamura, J., and Yoshimi, K., Microstructure, high-temperature deformability and oxidation resistance of Ti₅Si₃-containing multiphase MoSiBTiC alloy, *Intermetallics*, 2017, vol. 90, pp. 169–179.
 68. Wang, J., Li, B., Li, R., Wang, T., Chen, X., and Zhang, G., Improved oxidation resistance of Mo–12Si–8.5B composite at 1400°C due to development of Zr-rich borosilicate scale, *Ceram. Int.*, 2019, vol. 45, no. 3, pp. 3111–3117.
 69. Kumar, N.K., Das, J., and Mitra, R., Effect of Zr addition on microstructure, hardness and oxidation behavior of arc-melted and spark plasma sintered multiphase Mo–Si–B alloys, *Metall. Mater. Trans. A*, 2019, vol. 50, pp. 2041–2060.
 70. Ouyang, G., Ray, P.K., Thimmaiah, S., Kramer, M.J., Akinc, M., Ritt, P., and Perepezko, J.H., Oxidation resistance of a Mo–W–Si–B alloy at 1000–1300°C: The effect of a multicomponent Mo–Si–B coating, *Appl. Surf. Sci.*, 2019, vol. 470, pp. 289–295.
 71. Litovchenko, S.V., Beresnev, V.M., Drobyshevskaya, A.A., and Turbin, P.V., Silicide coatings on molybdenum: Preparation, structure, properties, *Fiz. Inzh. Poverkhnost.*, 2012, vol. 10, no. 2, pp. 111–137.
 72. Perepezko, J.H., Sossaman, T.A., and Taylor, M., Environmentally resistant Mo–Si–B-based coatings, *J. Therm Spray Technol.*, 2017, vol. 26, pp. 929–940.

73. Choi, K., Yang, W., Baik, K.-H., Kim, Y., Lee, S., Lee, S., and Park, J. S., Growth kinetics and isothermal oxidation behavior of a Si pack cementation-coated Mo–Si–B alloy, *Appl. Surf. Sci.*, 2019, vol. 489, pp. 668–676.
74. Kolobkov, A.S. and Malakhovskii, S.S., Self-healing composite materials (review), *Tr. Vseross. Inst. Aviats. Mater.*, 2019, no. 1 (73), pp. 47–54.
<https://doi.org/10.18577/2307-6046-2019-0-1-47-54>,
<http://www.viam-works.ru> (Accessed January 15, 2020).
75. Yang, W., Choi, K., Baik, K.-H., Kim, Y., Lee, S., Lee, S., and Park, J.S., Oxidation behaviors of Si/Al pack cementation coated Mo–3Si–B alloys at various temperatures, *Met. Mater. Int.*, 2019, vol. 27, no. 5, pp. 914–921.
<https://doi.org/10.1007/s12540-019-00471-4>
76. Choi, K., Yang, W., Baik, K.-H., Kim, Y., Lee, S., Lee, S., and Park, J.S., Growth kinetics and isothermal oxidation behavior of aluminide pack coating on a multiphase Mo–Si–B alloy, *Oxid. Met.*, 2019, vol. 92, pp. 423–437.
77. Svetlov, I.L., Karpov, M.I., Neuman, A.V., and Stroganova, T.S., Temperature dependence of the ultimate strength of in situ multicomponent Nb–Si–*X* (*X* = Ti, Hf, W, Cr, Al, Mo) composites, *Russ. Metall. (Metally)*, 2018, vol. 2018, pp. 348–353.
<https://doi.org/10.1134/S0036029518040171>
78. Cormen, S.G. and Lutra, K.L., Development history of GE's prepreg melt infiltrated ceramic composite material and application, *Compr. Compos. Mater. II*, 2018, vol. 5, pp. 325–328.

Translated by K. Gumerov